# Small-Angle X-Ray Scattering of Aggregated DNA-Capped Colloidal Gold

A Thesis

Presented to the Faculty of the Graduate School

of Cornell University

In Partial Fulfillment of the Requirements for the Degree of

Master of Engineering

by

Mark Richard Hartman

August 2008

ABSTRACT

Nanoparticles conjugated with DNA ligands possess 1) assembly behavior that might be controlled by DNA length and sequence, as well as the presence of other ligands, and 2) material properties determined by the nanoparticle size, shape, and chemical identity. The combination of these features could allow for the production of novel materials with unique or useful properties. Previous work has demonstrated the application of DNA-capped gold nanoparticles for colorimetric DNA detection, and ordered assemblies of DNA-capped gold nanoparticles have also been reported. Here, small-angle x-ray scattering (SAXS) from a synchrotron source was used to characterize ordered assemblies of DNA-capped gold nanoparticles. The extracted structure factor obtained from these diffraction experiments confirmed the assembly of gold nanoparticles into crystallites with well-defined internal order, demonstrating the formation of a face-centered cubic (FCC) crystal lattice structure. Applying basic principles of x-ray diffraction such as the Scherrer Formula, the interparticle spacing and average size of crystallite aggregates were determined. The experimental approach outlined in this work may lead to the synthesis of programmable materials with unusual optical or electrical properties or controllable self-assembled topology. The ultimate goal of research in these types of DNA-capped colloidal systems is the development of a modular "toolkit" approach for nanoparticle self-assembly.

BIOGRAPHICAL SKETCH

Mark Hartman received his B.S. in Chemical Engineering from Cornell University.

I would like to thank Professor Dan Luo, Professor John March, Wenlong Cheng, Nokyoung Park, Detlef Smilgies, Ruipeng Li, & Karthik Sekar.

This work is based upon research conducted at the Cornell High Energy Synchrotron Source (CHESS), which is supported by the National Science Foundation under NSF award DMR-0225180, using the Macromolecular Diffraction at CHESS (MacCHESS) facility, which is supported by award RR-01646 from the National Institutes of Health, through its National Center for Research Resources.

TABLE OF CONTENTS

Chapter 1: Colloidal Crystallization of Gold Nanoparticles with DNA Linkers ..... 1

Chapter 2: X-ray Diffraction ..... 5

Chapter 3: Materials and Methods ..... 12

Chapter 4: Results and Discussion ..... 16

Chapter 5: Conclusions and Outlook ..... 26

Appendix A: Form Factor Simulation ..... 27

Appendix B: Face-Centered Cubic (FCC) Structure Factor Simulation ..... 28

Appendix C: Determination of Average Gold Nanoparticle Radius ..... 29

Appendix D: Estimation of DNA-Capped Gold Nanoparticle Interparticle Spacing ..... 30

# LIST OF FIGURES

Illustration of Bragg's Law ..... 8

Scheme of DNA-capped gold nanoparticle conjugation ..... 13

Scheme of set-up for SAXS characterization ..... 14

2-D detector images ..... 15

Conversion to 1-D integrated plot ..... 16

Comparison between intensity plot and form factor plot ..... 18

Comparison between simulated and experimental form factor ..... 19

Influence of particle radius on simulated form factor ..... 20

Influence of polydispersity on simulated form factor ..... 21

Structure factor ..... 22

Comparison between experimental and simulated structure factor ..... 23

FCC unit cell and (111) planes ..... 24

Histogram of gold nanoparticle radii ..... 29

CHAPTER 1

# Colloidal Crystallization of Gold Nanoparticles with DNA Linkers

## *Overview*

Organizing nanoparticles into defined structures with controlled inter-particle spacing remains a daunting challenge. DNA has shown some promise in this area, due to its programmability and well-characterized structural properties. Using DNA as "linkers" for gold nanoparticles forms a modular approach to materials synthesis by self-assembly, combining the specificity of Watson-Crick base-pairing with the versatile properties of nanoparticles.

## *DNA-Capped Gold Nanoparticles*

Due to the ease of preparation, chemical stability, and straightforward functionalization of gold nanoparticles, work involving DNA-conjugated nanoparticles has developed primarily around colloidal gold. Mirkin et al. first described the reversible self-assembly of 13-nm DNA-conjugated gold nanoparticles into polymeric aggregates in 1996.[1] In this original system, two batches of gold nanoparticles were labeled with two different oligonucleotides. The DNA-gold conjugates were obtained by reacting the gold nanoparticles with a thiol functional group added to the 5' end of single-stranded DNA. Each of the two sequences was semi-complementary to a target DNA sequence. When this target DNA was added to the solution, both semi-complementary oligonucleotides hybridized to the target strand to form stable duplexes. The attractive forces of DNA hybridization were sufficient to assemble the gold nanoparticles into polymeric aggregates. This aggregation was temperature sensitive and reversible; if the mixture was heated over the melting point ($T_m$) of the hybridized DNA, then the DNA-conjugated gold

nanoparticles re-dispersed into solution. The assembly of gold nanoparticles accompanied a reversible color change from red (absorbance at 520nm) to blue (absorbance 600 to 700nm), an optical effect resulting from the change in interparticle distance.

In contrast to the approach of Mirkin et al., in which many oligonucleotides were used to label each 13-nm gold nanoparticle, Alivisatos et al. demonstrated a similar system with only one DNA oligonucleotide conjugated to each gold nanoparticle while using gold nanoparticles with a smaller diameter of 1.4 nm.[2] These gold nanoparticles were functionalized with one maleimide substituent per nanoparticle, and this maleimide was coupled to a thiol at either the 5′ or 3′ end of single-stranded DNA. The resulting DNA-labeled gold nanoparticles hybridized to complementary single-stranded DNA oligonucleotides. Rather than forming large polymeric aggregates of gold nanoparticles, the authors opted for a smaller-scale approach, demonstrating the dimerization and trimerization of individual gold nanoparticles. The formation of these hybrid structures was confirmed by TEM, and the distance between nanoparticles was in agreement with the calculated length of DNA. Since the authors attempted both 5′ and 3′ labeling, both head-to-tail (antiparallel) and head-to-head (parallel) duplex configurations were possible. The authors suggested that "codons" corresponding to different types or sizes of nanoparticles could be encoded into the template strand, potentially allowing for the addressable assembly of designer materials.

In addition to DNA length and sequence, the role of rigidity of the DNA on the gold nanoparticle surface has also been explored.[3] Single-stranded DNA was added to DNA-conjugated gold nanoparticles (~9.6 nm) in order to form partial duplexes,

resulting in a more rigid DNA on the gold nanoparticle surface and a larger effective particle size. This increase in DNA rigidity along the gold nanoparticle surface increased the kinetics of binding between gold nanoparticles, as shown in TEM images and UV-vis spectra. In a similar manner, a mixture of non-complementary and complementary DNA has been conjugated to gold nanoparticles, resulting in a smaller average size of polymerized nanoparticle aggregates and a lower observed $T_m$.[4] The authors suggest that introducing these irrelevant oligonucleotides introduced some steric clash, thermodynamically disfavoring hybridization. This experiment was repeated on the micro-scale with 1.9 μm polystyrene beads with similar results. The authors cite this experiment as a means to control the relative contributions of attractive and repulsive forces. The irrelevant, non-bonding DNA used in this study could be replaced with another set of complementary DNA specifically to form another linkage to add more components or sizes to the system.

***Crystallization of DNA-Capped Gold Nanoparticles***

Recently, two groups have independently demonstrated the self-assembly of ordered three-dimensional arrays of DNA-conjugated gold nanoparticles.[5,6] Park et al.[5] designed a system in which gold nanoparticles are conjugated to single-stranded DNA oligonucleotides, as in previous schemes. As in Mirkin's usual approach, a double-stranded DNA linker is then added to this system, which encodes a long single-stranded region complementary to the DNA sequences on the nanoparticles. This linker also includes a one-base pair "flexor" which introduces some flexibility into the hybridized structure. The result of this configuration after hybridization is an ordered, three-dimensional nanoparticle array, in the form of a face-centered cubic (FCC) crystal structure. If two different partially complementary linkers are used instead of one partly self-complementary linker, the nanoparticles adopt a body-

centered cubic (BCC) configuration. These structures of the obtained crystallites were demonstrated with small-angle x-ray scattering (SAXS), and the lattice structures were shown to be reversible over multiple heating and cooling cycles through the $T_m$.

Similar results were obtained without the use of an additional "target" or "linker" strand.[5,7] Here, two batches of single-stranded DNA nanoparticles, each encoding sequences complementary to the other, were mixed together to form an ordered assembly. A flexible region was included in the form of a "spacer" between the nanoparticle and the overlapping hybridized region. Though the authors caution that SEM conditions might not preserve the crystalline structure, they present SEM images that confirm the assembly/disassembly of aggregates above and below the $T_m$. The authors emphasize that, in this system, the role of DNA is "assembler" while the nanoparticles compose the bulk of the crystal and determine its properties. Thus, this approach may be a powerful and generic technique for assembling a variety of hybrid three-dimensional crystalline assemblies.

CHAPTER 2

# X-ray Diffraction

## *Production and Scattering of X-Rays*

X-rays fall between gamma rays and UV rays in the electromagnetic spectrum, with wavelengths roughly between 0.01 and 100 A. Due to this small wavelength (length scale similar to inter-atomic bonds), x-rays can produce diffraction patterns when they pass through a crystal. These diffraction patterns can reveal information about the internal structure of the crystal.

X-rays are produced by a rapidly accelerating or decelerating charge. In practice, this is usually achieved by accelerating electrons with a high voltage into a metal target. This approach produces a large amount of heat and a small quantity of x-rays. The resulting x-rays will possess a distribution of wavelengths according to 1) a continuous spectrum and 2) a characteristic spectrum. The continuous spectrum arises from Bremmstrahlung (braking radiation), produced from the deceleration of electrons colliding with the metal target. The characteristic spectrum arises from the "knocking away" of electrons within the metal target by the accelerated (external) electrons; the lost electrons are replaced by other electrons within the metal atoms, releasing energy that corresponds to spectral lines characteristic of the metal. Both types of spectra exhibit a dependence on the accelerating voltage. The strong, sharp peaks from the characteristic spectrum (in particular, the $K\alpha_1$ peak of molybdenum) are often utilized in x-ray diffraction studies, in which monochromatic x-rays are often preferred.

Alternately, x-rays can be produced from a synchrotron. In a synchrotron, instead of impinging electrons against a metal target, electrons are accelerated to high speeds and then circulated around a ring under the control of powerful magnets. This circular acceleration of electrons produces a steady supply of x-rays. Generally, synchrotron sources generate x-rays with higher intensity over a broader range of accessible wavelengths than those from smaller-scale systems.

When a beam of x-rays strikes a solid material, the x-rays are partially transmitted and partially absorbed (either by scattering or by true absorption), depending on the wavelength of the x-rays and on the identity of the solid material. In most cases, only a small fraction of the incident x-rays are scattered, but only these scattered x-rays can reveal the internal structure of the solid material. More specifically, when an x-ray beam strikes a solid material, two types of scattering events can occur: coherent scattering, which reveals useful structural information about the material, and incoherent scattering, which is pretty much useless. Coherent scattering occurs when an x-ray beam strikes a tightly bound electron and causes it to oscillate, creating another x-ray beam with the same wavelength and phase as the incident beam. Coherent scattering can occur in any direction, but its intensity decreases as theta (the complement of the angle of reflection, see Figure 1) increases. Alternately, incoherent (termed "Compton-modified scattering") occurs when an x-ray beam strikes a loosely bound electron and gives it some kinetic energy; the x-ray beam loses the energy imparted to the electron and suffers a corresponding increase in its wavelength. This type of scattering becomes more likely with decreasing atomic number Z (because smaller atoms have a weaker hold on their electrons). Thus, light elements such as carbon, hydrogen, and oxygen tend to appear "noisy" in x-ray diffraction experiments.

***Bragg's Law***

Any wavelength of electromagnetic radiation can undergo diffraction, which occurs as a result of interference between electromagnetic waves. This interference can be either constructive or destructive. For example, two monochromatic waves with equal intensity and wavelength can form a wave with the same wavelength and twice the intensity, or they can cancel either completely. Maximum intensity occurs when both component waveforms are out-of-phase by some integer multiple of their wavelength, and zero intensity occurs when they are out-of-phase by some integer multiple of ½ their wavelength. In general, shifting the phase of either component wave with respect to the other will either amplify or attenuate the overall signal.

X-ray diffraction applies this concept to waveforms that: 1) initially, travel along the same path, in phase and with the same wavelength (i.e. from an x-ray source), 2) take different paths (i.e. undergo scattering through a well-ordered crystal lattice), and then 3) re-unite along identical paths again (i.e. as the x-rays travel from the crystal to the detector). At the detector, some of these diffracted rays will constructively reinforce each other, while others will destructively cancel each other.

Bragg's Law describes the condition that must be met for constructive reinforcement of scattered x-rays (Figure 1). Specifically, Bragg's Law describes the relationship between the path length of an x-ray beam within a crystal lattice and the resulting phase shift of the beam (Equation 1).

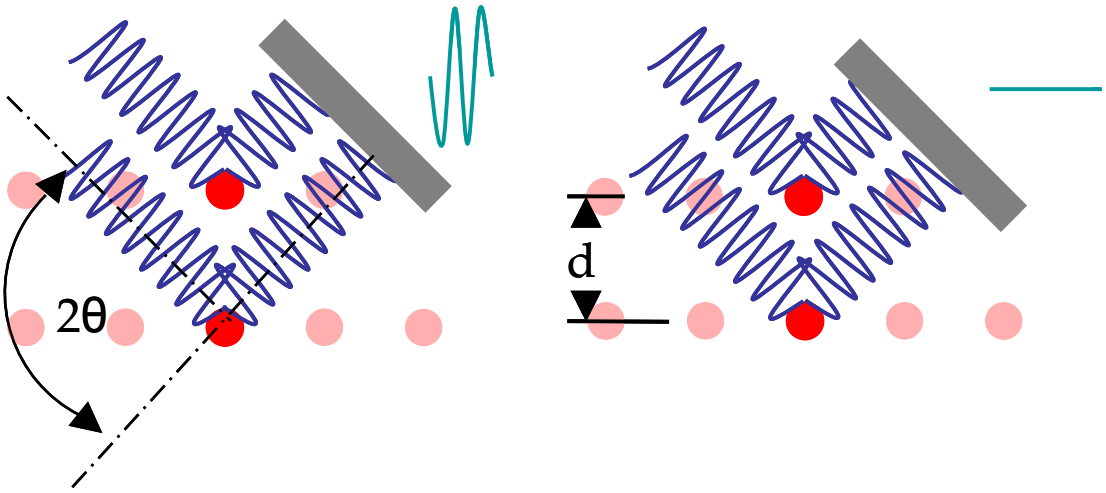


**Figure 1**: Illustration of Bragg's Law. Depending on the difference in overall distance traveled by two initially coherent waveforms, they can interfere constructively or destructively.

$$n\lambda = 2d \cdot \sin\theta$$

**Equation 1**: Bragg's Law, in which n: any integer, λ: wavelength, d: distance between Bragg planes, θ: angle between incident beam and Bragg plane

If the extra distance traveled by an x-ray beam is equal to some integer multiple of its wavelength, then reinforcement can occur. Since this extra distance corresponds to the spacing between planes in the crystal lattice, Bragg's Law allows for the calculation of inter-atomic spacing when both the wavelength of the x-ray beam and incident angle are known. Bragg's Law is a necessary, but not sufficient, condition for constructive interference, since certain crystal orientations might prevent effective reinforcement. Additionally, even if constructive interference successfully occurs,

there is no guarantee that the detector will be sensitive enough to distinguish the resulting signal.

Due to the restriction of Bragg's Law, a monochromatic beam of x-rays will, in general, produce no diffraction pattern. To study a sample with unknown inter-atomic spacing, a method must be applied to systematically vary the parameters in Bragg's Law (wavelength and incident angle). In practice, three alternate methods are the most popular: the Laue method, the rotating crystal method, and the powder method. The Laue method uses "white" x-rays with a broad distribution of wavelengths to interrogate the sample, which has a fixed incident angle theta. Since virtually every possible wavelength of x-ray strikes the sample, Bragg's Law is likely to be satisfied in at least some cases. Every diffracted beam has a different wavelength, and produces a spot on the detector. The rotating crystal method uses a monochromatic x-ray beam but varies theta (angle between the incident beam and Bragg plane) to a similar effect. The powder method requires breaking the crystal of interest into a coarse powder, in which each particle of powder is a tiny crystallite randomly orientated with respect to the incident beam. Thus, by sheer force of numbers, some pieces of the powder will be aligned in a way that satisfies Bragg's Law.

***Results Obtainable by X-ray Diffraction***

Diffraction peaks are often considered to occur as a result of constructive interference, but they can also be considered as a result of destructive interference. In other words, Bragg's Law is satisfied not only when constructive interference occurs, but also when destructive interference fails to occur. This leads to a relationship between the diffraction peak broadening and crystallite size.[9-12] This relationship is the Scherrer

equation, which allows crystal size to be estimated from an x-ray diffraction pattern (Equation 2).

$$t = \frac{K\lambda}{FWHM \cos\theta}$$

**Equation 2**: Scherrer equation, in which FWHM: full-width half-max, K: Scherrer constant (approx. 1), λ: wavelength, t: crystallite thickness, θ: angle between incident beam and Bragg plane

For a crystal of infinite size, every scattered wave has a "partner" that was scattered from an adjacent particle and is phase-shifted by some amount; thus, every scattered wave that does not satisfy Bragg's Law undergoes some destructive interference with another scattered wave. However, for a finite crystal, scattered waves at the boundary of the crystal will be missing some of their "partners." Thus, the amount of destructive interference that can occur is reduced, and the diffraction peaks resulting from constructive interference become relatively less distinct.

Besides providing information about interparticle spacing and structure, x-ray diffraction patterns also contain information about the shapes of the constituent particles. A diffraction pattern from a typical x-ray diffraction experiment can be considered as a combination of two component diffraction patterns. The diffraction pattern produced by Bragg's Law is the Structure Factor (SF), and the diffraction pattern produced by particle shapes is the Form Factor (FF). In an x-ray diffraction experiment, both the SF and the FF contribute to produce intensity peaks (Equation 3).

$$I(q) = FF(q) \cdot SF(q)$$

**Equation 3**: The simple relationship between form factor (FF), structure factor (SF), and intensity (I)

The form factor contains information about particles' radii, shapes, and polydispersity; it can be observed experimentally at low particle concentrations when the particles do not form structure (SF = 1). In order to better analyze the SF, it is often necessary to divide out the FF.

The isolated structure factor presents a pattern of diffraction peaks that may correspond to a particular lattice structure. In theory, particles can only form a finite number of types of ordered assemblies, although a vast number of complexities and deviations can arise. All the possible lattice structures have already been discovered and studied, and their corresponding diffraction patterns are already known. Thus, identifying the lattice structure of an unknown sample is often a matter of comparison against known standards. Since a material's lattice structure plays some role in determining its bulk properties, identification of the crystal lattice is an important outcome of x-ray diffraction experiments.

Lattice identification is based on the concept of the unit cell. A crystal lattice is composed of a single repeating component, the unit cell, and this unit cell, in turn, is composed of particles (i.e. atoms or molecules). There are a finite number of arrangements that unit cells can adopt, and all have been well studied and categorized by crystallographers. The particles within the unit cell define many possible planes, each of which can be uniquely identified by crystallographic notation. Bragg's Law refers to the distances between these planes, and parallel planes with an inter-plane distance that satisfies Bragg's Law are termed Bragg planes. X-ray diffraction allows us to identify the Bragg planes within a crystal, and this information allows us to determine the type of unit cell that comprises the crystal.

CHAPTER 3

# Materials and Methods

## *Preparation of DNA-capped Gold Nanoparticles*

Gold nanoparticles with 12 nm diameter were prepared according to the Turkevich method.[8] First, 5.0 μmol $HAuCl_4$ was dissolved in 19 mL DI water to produce a yellowish solution. This solution was heated to boiling, and 1 mL 0.5% sodium citrate was added. The sodium citrate acted as a reducing agent and also introduced negative charge-charge repulsion that prevented aggregation of the nanoparticles. Less sodium citrate produces larger nanoparticles; the amount of charge-charge repulsion available per unit surface area decreases, and smaller nanoparticles will therefore aggregate until their surface area is small enough for the sodium citrate to play a stabilizing role. While still being heated, the solution was vigorously stirred for 30 minutes, after which its color had changed to wine-red. The resulting nanoparticles were monodisperse and spherical with an average diameter of 12 nm, as confirmed by TEM (data not shown).

The gold particles were capped with DNA by a procedure similar to Mirkin et al.[1] Oligonucleotides, functionalized with 5′-end alkyl-disulfide, were deprotected and incubated with 0.8 mL of the gold nanoparticle solution prepared as above. This incubation occurred at room temperature for 12 hours. Then, sodium chloride was added to a final concentration of 0.2 M. This solution was aged for another 12 hours in order to further increase the surface density of DNA. Finally, the solution was centrifuged and exchanged with MilliQ water. If necessary, the amount of unconjugated DNA could be further reduced by repeating these centrifuge and buffer exchange steps. The UV-VIS spectra of resulting solutions were measured, and

absorbance peaks at 260 nm indicated the successful conjugation of DNA to the gold nanoparticles.

The resulting gold nanoparticles were capable of self-assembly due to the stabilizing effect of the DNA ligand. The DNA introduces favorable hydrogen bonds in the form of Watson-Crick base pairing. The DNA sequence used in this experiment was palindromic, potentially allowing for specific hybridization between DNA ligands (Figure 2).

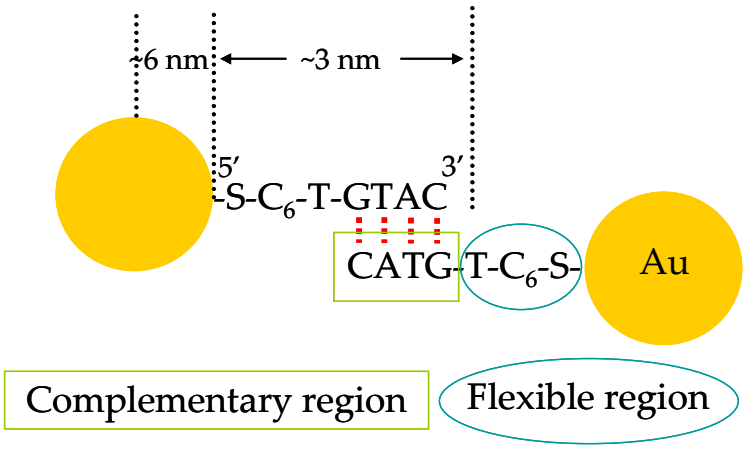


**Figure 2:** Scheme of DNA-capped gold nanoparticle conjugation, in which S and $C_6$ refer to thiol and alkyl linkages, respectively. In reality, multiple ligands exist per particle. Illustration is not to scale; approximate dimensions are indicated.

***SAXS Characterization of DNA-capped Gold Nanoparticle Solution***

The ordered structure within self-assembled aggregates of DNA-capped gold nanoparticles was then explored by x-ray diffraction. For analyzing samples containing large (nanometer-scale) particles suspended in solution, small-angle x-ray scattering (SAXS) is commonly used. In SAXS, the small theta angle of the incident beam is required to analyze large interparticle distances, as is obvious from Bragg's Law (Equation 1).

$$n\lambda = 2d \cdot \sin\theta$$

**Equation 1**: Bragg's Law, in which n: any integer, $\lambda$: wavelength, d: distance between Bragg planes, $\theta$: Bragg angle

The particles can spontaneously assemble to form small crystallites within the solution. Although most x-ray diffraction experiments deal with dry samples, the standard powder method can be applied to nanometer-scale particles in solution without significant modification.

Using a modification of standard solution-phase SAXS, x-ray diffraction experiments were carried out to analyze the crystalline structure of DNA-capped gold nanoparticles. For these experiments, a droplet of solution containing DNA-capped gold nanoparticles was placed on Kapton (polyimide virtually transparent to x-rays) tape, and both the tape and the droplet were oriented perpendicular to the path of the incident x-ray beam. Under these conditions, DNA-capped gold nanoparticles could be observed at various stages of drying (Figure 3).

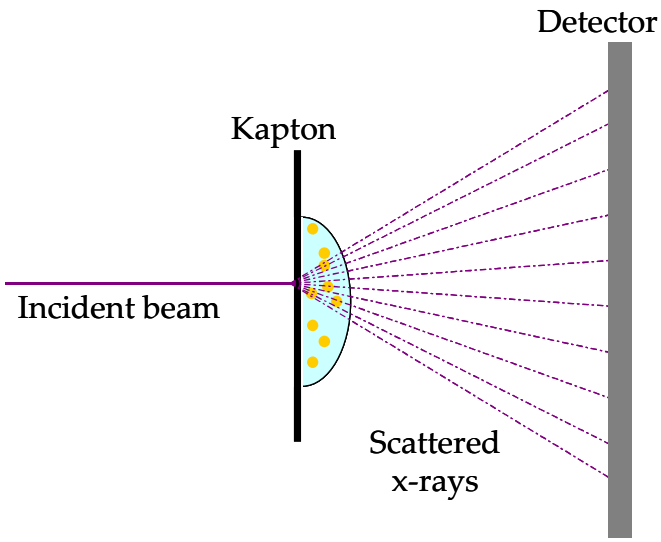


**Figure 3**: Scheme for SAXS characterization of a solution containing DNA-capped gold nanoparticles.

The scattered x-rays were collected by a CCD detector and processed into a digital format. The resulting data file contains the x-ray intensity accumulated at each pixel, which can be displayed as a high-resolution image with color-coded intensity information (Figure 4). Initial stages of data processing were carried out with the software FIT2D.[13]

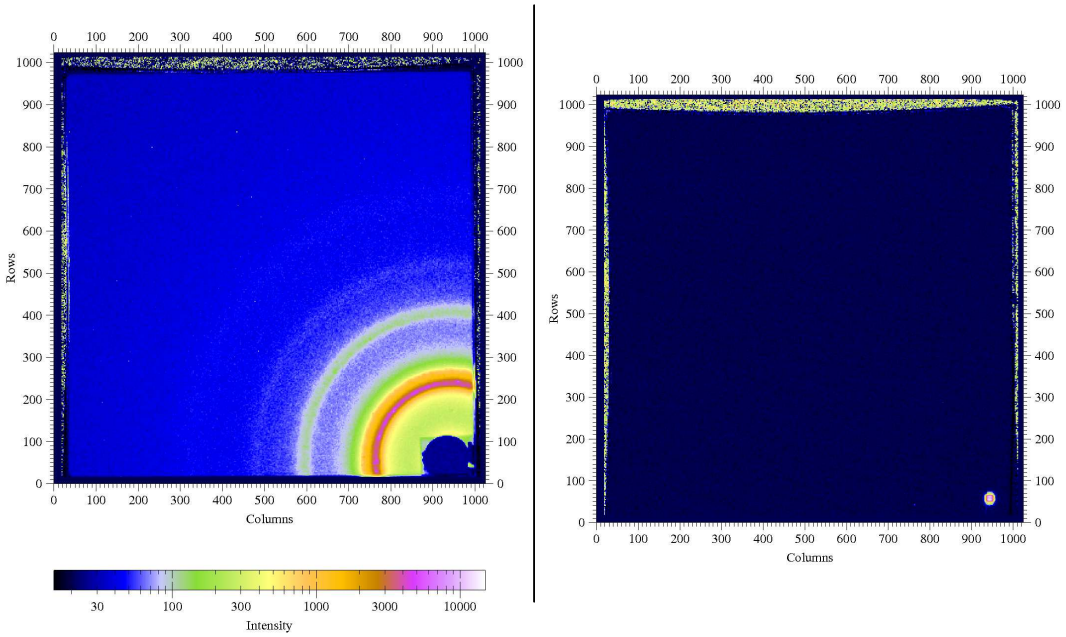


**Figure 4**: Raw detector data converted to digital images. Left: Image from typical sample with rings corresponding to Bragg angles. The blue circle in the lower-right corner is the beam stop. Intensity is encoded as color information; the intensity scale is shown. Right: Detector image of direct beam, without sample or beam stop. During a typical measurement with a sample, this direct beam would overwhelm the CCD if the beam stop were not in place. Here, the beam was weakened to prevent damage to the detector.

This image shows concentric rings, with radii of twice the Bragg angle θ (2-theta). These rings indicate the 2-theta values at which Bragg's Law is satisfied (this is an oversimplification, but is more or less true). The rings are centered at 2-theta = 0, which is defined as the location of the direct beam). While analyzing samples, a beam stop prevents the direct beam from striking the detector.

CHAPTER 4

## Results and Discussion

### *Integration of the Detector Image*

The raw data gathered by the CCD detector contains all the information from a single x-ray diffraction experiment, but further processing is required to extract useful results. The intensity at each pixel depends upon the intensity of the incident beam and the exposure time, and so the raw data must be normalized by the accumulated intensity of the incident beam. This allows for the comparison of data taken from different samples and exposure times. Next, the original image can be converted into a plot of intensity vs. 2-theta by radial integration over the normalized data (Figure 5).

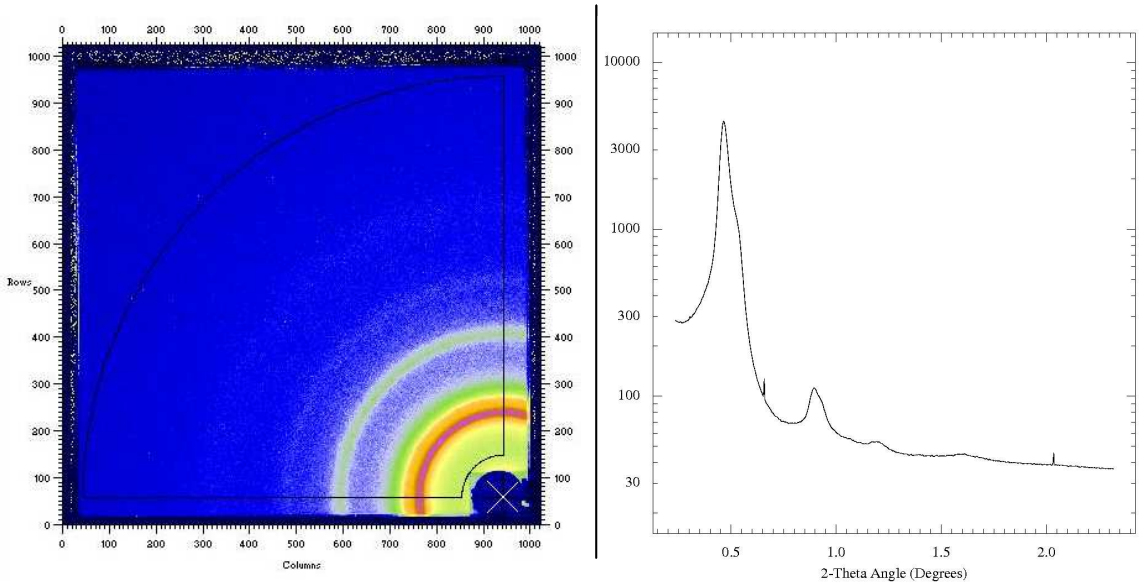


**Figure 5**: Radial integration of raw detector data to construct a plot of intensity vs. 2-theta. Left: Integration limits of the raw detector data. Right: Resulting two-dimensional plot, in which the Y-axis is in units of arbitrary intensity (au). Integration was performed by the program Fit2d.[13,14]
The features at 2-theta = 0.65 and 2.05 are artifacts, due to "noisy" pixels in the CCD detector. They will be removed at a later stage in the processing.

In order to simplify further calculations and allow for general comparisons between samples and theory, 2-theta should be replaced with a more convenient unit, q (Equation 4). These q values take both the wavelength of the incident beam and the path distance into account. The units of q-space are inverse nanometers ($nm^{-1}$), and there is a simple relationship between q and the distance between Bragg planes (d) (Equation 5).

$$q = \frac{4\pi}{\lambda} \cdot \sin\theta$$

**Equation 4**: Relationship between q and θ, in which q: units of reciprocal space, λ: wavelength, θ: angle between incident beam and Bragg plane.

$$q = \frac{2\pi}{d}$$

**Equation 5**: Relationship between q and d derived from Bragg's law, in which q: units of reciprocal space, λ: wavelength, θ: angle between incident beam and Bragg plane.

***Extracting the Form Factor***

The intensity in this integrated plot is a product of two factors: 1) a structure factor (SF) which contains information about the particles lattice structure, inter-particle distance, and crystallite size, and 2) a form factor (FF) which contains information about the particle shape. For any given q, the product of these factors yields the observed intensity (I) (Equation 3). Thus, in order to accurately analyze the structure factor, the form factor must be identified and extracted. The form factor can be determined experimentally or theoretically.

$$I(q) = FF(q) \cdot SF(q)$$

**Equation 3**: The simple relationship between form factor (FF), structure factor (SF), and intensity (I).

The experimental approach to determining the form factor depends on particle concentration. Below a threshold concentration of particles, no crystal lattice structure is formed; instead, the particles exist as dispersed solutes. Thus, at low particle concentrations, no structure factor is present and only the form factor can be observed. This is consistent with our experimental data: integrated plots of our sample at low concentrations are markedly different from plots of otherwise similar samples at higher concentrations (Figure 6).

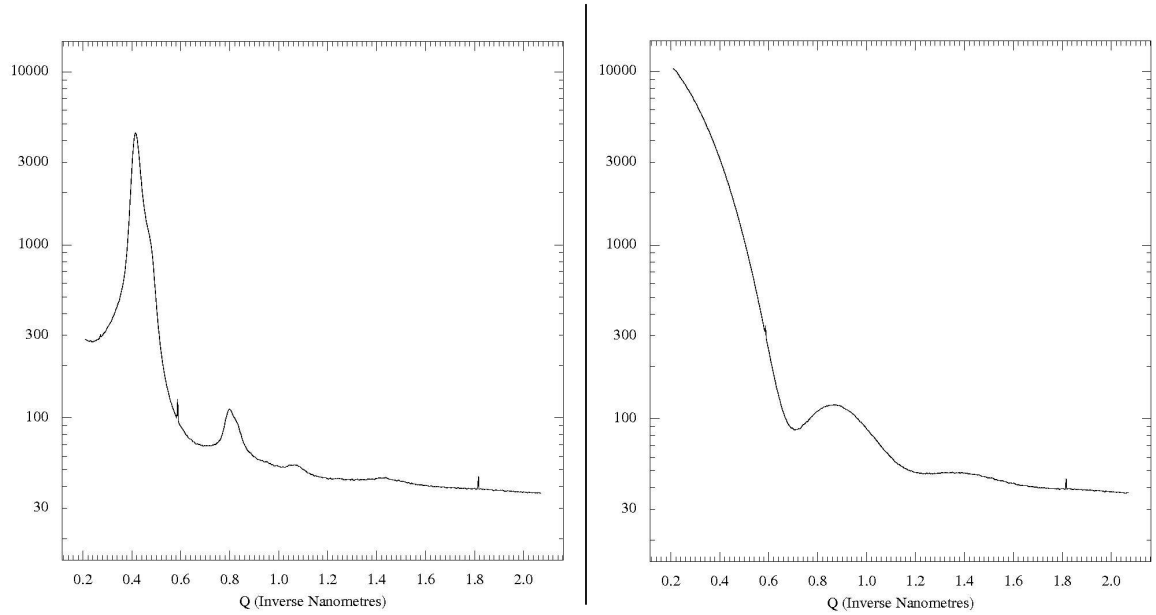


**Figure 6**: Comparison of integrated plots corresponding to high and low nanoparticle concentrations. Left: High concentration exhibits peaks due to both structure factor (SF) and form factor (FF). Right: Low concentration exhibits peaks only due to FF.

We can confirm these observations by comparison of our form factor (FF) with theory. Our gold nanoparticles are approximately spherical, with dimensions similar to the wavelength of the x-rays. Under these conditions, the scattering of light from a

sphere is well understood, and obeys a fundamental formula first derived by Rayleigh in 1911 (Equation 6).[12,15]

$$F(q) = \left[ 4\pi \cdot R^3 \cdot \frac{\sin(Rq) - Rq\cos(Rq)}{(Rq)^3} \right]^2$$

**Equation 6**: The theoretically derived spherical FF function

Applying the known equation for theoretical scattering from a sphere, we can simulate a hypothetical FF that is in good agreement with the experimentally observed FF (Figure 7). Details of the FF simulation are given in Appendix A; this simulation was performed with MATLAB.

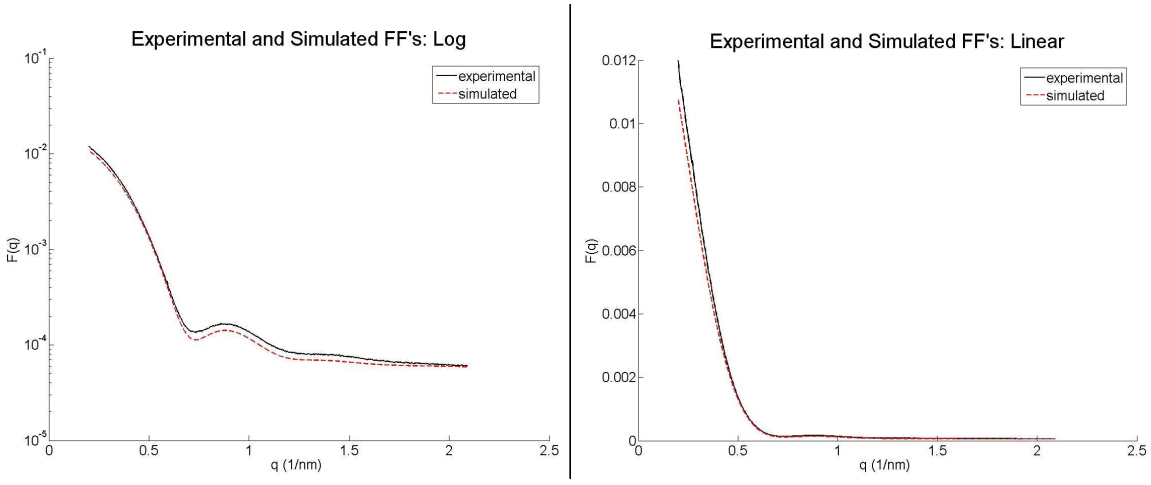


**Figure 7**: Comparison between simulated and experimentally observed FF. Both log and linear plots are shown, as they display different features of the FF function.

Characteristics of the simulated and experimental FF curves give additional information about the particle radius and polydispersity within our samples. The simulated FF and experimental FF are well-fit with a simulated average particle radius of 6.1 nm, 90% of the average 6.7 nm radius observed by TEM (Appendix C). Modifying this parameter in the FF simulation results in deviations from our experimental result in terms of number and placement of peaks (Figure 8).

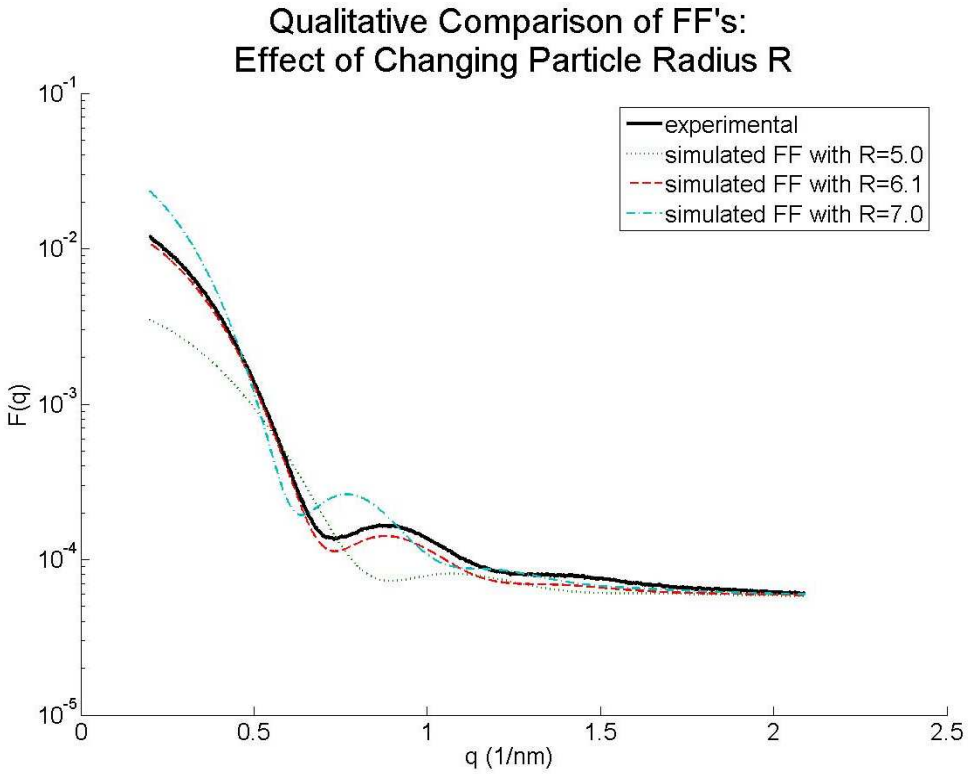


**Figure 8**: Sensitivity of simulated form factor to input value of particle radius.

We observed at least two clear peaks in the FF, corresponding to a relatively monodisperse sample. The simulated FF is based on a Gaussian distribution of particle radii with a standard deviation of 0.70 nm. This amount of polydispersity is consistent with TEM observations, which give a standard deviation of 0.64 nm (data not shown). A polydisperse sample would produce a FF with flatter, broader oscillations (Figure 9).

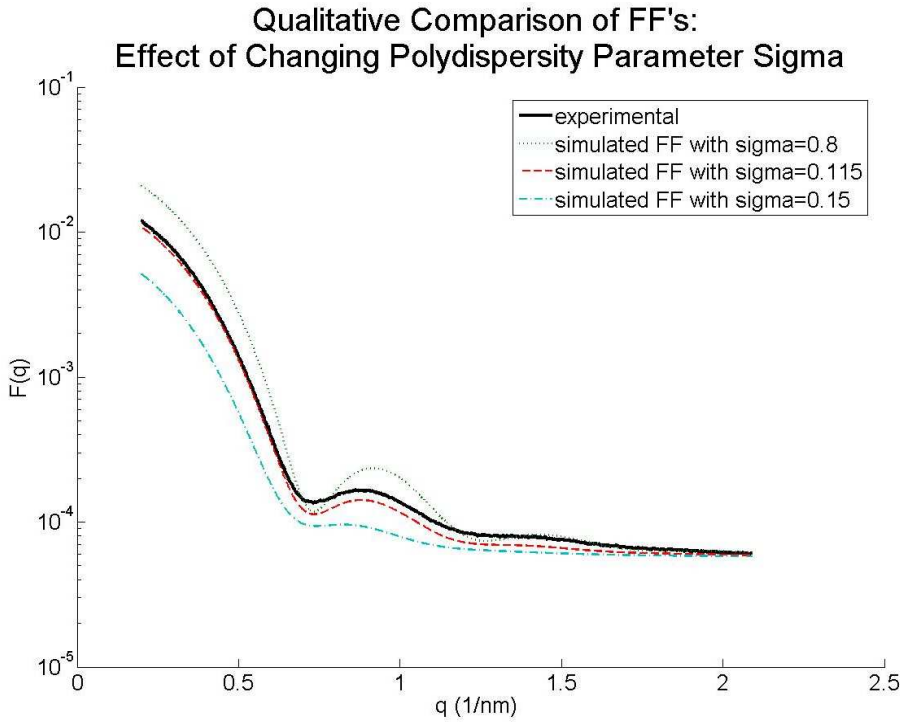


**Figure 9**: Sensitivity of simulated form factor to value of particle size distribution.

***Analysis of the Structure Factor***

Once we successfully obtained the FF, we could then extract it from the integrated intensity plots and isolate the resulting structure factor (Figure 10). The presence of distinct, irregularly-spaced peaks suggests that the DNA-capped gold nanoparticles possess some type of structure. Since a good match was achieved between the

experimental FF and simulated FF, either the experimental FF or simulated FF could be extracted without affecting the outcomes of the downstream analysis. The experimental FF will be used from this point forward.

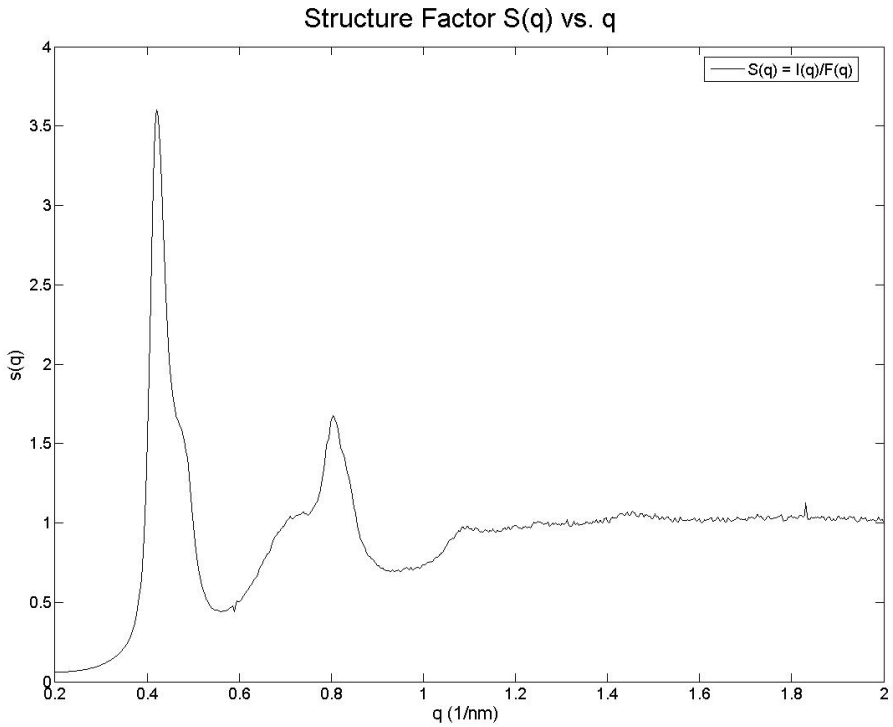


**Figure 10**: Structure factor resulting from original integrated plot (Figure 5) divided by the experimental FF.

The simplest conclusion to draw from the structure factor is the distance between the two closest Bragg planes in the lattice. Identifying the q value of the first peak of the structure factor and applying Equation 5, a value of 14.95 nm was calculated. This value corresponds to the nearest distance between Bragg planes.

$$q = \frac{2\pi}{d}$$

**Equation 5**: Relationship between q and d, in which q: reciprocal space units, d: spacing between Bragg planes

The lattice structure of the gold nanoparticles could then be identified. To aid in this analysis, it is helpful to divide all the x-axis by the q of the first peak (q0). This allows us to generalize across different samples, which may have different unit cell sizes. With units of q/q0 along the x-axis, all crystal lattices of the same structure should have identical diffraction peak patterns.

The q/q0 values at each peak were then identified and compared to the known diffraction peak sequences of various crystal lattice structures. The sequence of q/q0 values from the DNA-capped gold nanoparticles (1, 1.141, 1.691, 1.911, 1.968, 2.609) resembled part of the q/q0 sequence of a typical face-centered cubic (FCC) structure (1, 1.155, 1.632, 1.915, 2, 2.309, 2.517, 2.828). To allow for a more thorough comparison, the face-centered cubic (FCC) lattice structure was simulated with MATLAB (Appendix B). The resulting qualitative comparison between the simulated FCC and the unknown peaks strongly suggests that the DNA-capped gold nanoparticles self-assembled into an FCC configuration (Figure 11).

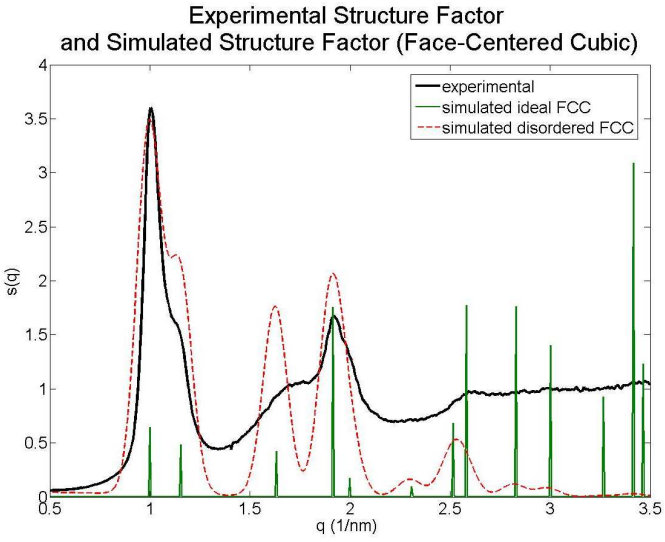


**Figure 11**: Comparison between experimental structure factor and simulated FCC structure factor.

With the conclusion that the structure is FCC, the size of the crystal lattice can now be determined by adapting the nearest neighbor distance to fit FCC geometry. Each peak in the structure factor corresponds to a particular set of Bragg planes. In the FCC structure, the first peak corresponds to the (111) plane (i.e. the distance between the two (111) planes within a single FCC unit cell, Figure 12). Applying some geometry, the distance between these two planes can be related to both the unit cell length (Equation 7) and the "nearest neighbor" interparticle spacing.

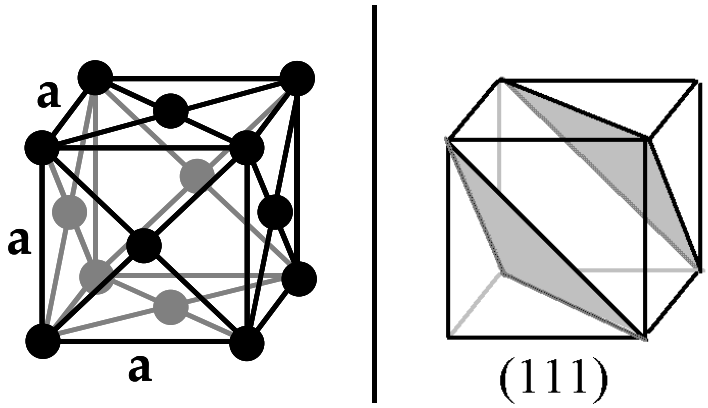


**Figure 12**: FCC unit cell. Left: Particle placement within FCC unit cell structure; unit cell side length (a) is shown. Right: (111) planes indicated within the FCC unit cell. These planes corresponding to the first diffraction peak in the FCC structure factor. The distance between these planes is given by Equation 7.

$$d = \frac{a}{\sqrt{3}}$$

**Equation 7**: Relationship between d and a, in which d: distance between Bragg planes, a: unit cell side length.

$$4R = \sqrt{2}a$$

**Equation 8**: Relationship between R and a, in which R: effective particle radius, a: unit cell side length. Interparticle spacing is 2R.

Applying this relationship to the known distance between (111) planes, 14.95 nm, we can determine that the unit cell length is 25.89 nm and the nearest neighbor

interparticle distance is 18.30 nm. This distance is within the range of values estimated from the radius of the gold nanoparticles plus the length of the ligand chain (17.3 - 20.9 nm, Appendix D).

The average crystallite size can also be estimated from the structure factor in Figure 9 by applying the Scherrer formula (Equation 2).

$$t = \frac{K\lambda}{FWHM \cos\theta}$$

**Equation 2**: Scherrer equation, in which FWHM: full-width half-max, K: Scherrer constant, $\lambda$: wavelength, t: crystallite thickness, $\theta$: Bragg angle

This formula relates peak broadening to crystallite size, a relationship that arises because the ratio between destructive interference and constructive interference is reduced for small crystallites. Applying the Scherrer formula to the first peak in Figure 9, the average crystallite "thickness" (along an average direction) was calculated as 130 nm. Considering the nearest neighbor interparticle distance (18.30 nm) a 130 nm crystallite could contain, at most, 7 nanoparticles across an average crystallite axis.

CHAPTER 5

## Conclusions and Outlook

DNA-capped gold nanoparticles were produced and their self-assembled structure was investigated by SAXS. Analysis of the structure factor indicates that this sample adopted an FCC lattice structure with interparticle spacing of 18.30 nm, and an average crystallite size of 130 nm. This system possesses a large number of easy-to-modify input parameters (i.e. nanoparticle size, shape, and chemical identity; DNA length and sequence; salt concentration) that might have a direct effect on parameters of crystallization (i.e. lattice structure, unit cell dimensions, size and stability of crystallites). These changes in crystallization behavior will potentially result in new materials with interesting or useful properties. The general approach presented here may serve as a blueprint for further exploration.

Ordered materials often possess unique properties, and DNA might be a convenient means of controlling the degree of ordering or type of ordering that occurs. Additionally, labeling different batches of particles with different sequences of DNA could allow for the production of new self-assembled materials with controllable properties. Progress in this area might be stimulated by current interest in metamaterials, nano-photonics, or other fields that could benefit from "designer" materials with tunable properties.

.

APPENDIX

*Appendix A: Form Factor Simulation*

The spherical form factor describes the intensity of diffracted light from a particle of radius R as a function of reciprocal space, q (Equation A1).

$$FF(q,R) = \left[ 4\pi \cdot R^3 \cdot \frac{\sin(Rq) - Rq\cos(Rq)}{(Rq)^3} \right]^2$$

**Equation A1**: Ideal spherical form factor, in which R: particle radius.

Accounting for polydispersity requires a probability density function, assigning a probability for a range of particle radii. Here, the Gaussian distribution function was chosen (Equation A2).

$$P(r) = \frac{\exp\left[ -\frac{1}{2}\left( \frac{r - R_0}{\sigma} \right)^2 \right]}{\sigma\sqrt{2\pi}}$$

**Equation A2**: Gaussian probability density distribution, in which $R_0$: average particle radius, $\sigma$: particle radius standard deviation. Here,

$$R_0 = 6.1, \sigma = 0.115 \cdot R_0$$

For each particle radius within a range of radii, the FF is calculated and weighted by the probability associated with that radius. These weighted FF's are then averaged (Equation A3).

$$AvgFF(q) = \frac{1}{N}\left\{ \sum_{i=0}^{N} P(r_{initial} + i \cdot r_{increment}) \cdot FF(q, r_{initial} + i \cdot r_{increment}) \right\}$$

**Equation A3**: Averaged FF, in which N: number of bins, $r_{initial}$: minimum radius, $r_{increment}$: step size factor. Here,

$$N = 20, r_{initial} = R_0 - 2.5 \cdot \sigma, r_{increment} = \frac{5 \cdot \sigma}{N}$$

Additionally, the simulated FF were scaled by a constant multiplier and shifted by a constant intensity as follows: $Yscale = 1.056E-7, Yshift = 5.70E-5$

*Appendix B: Face-Centered Cubic (FCC) Structure Factor Simulation*

Determining the diffraction peaks of a crystal lattice requires summing the contributions of the scattered waves from each atom in the lattice (Equation B1). This equation also includes a term (w) to account for the broadened peaks that occur from any non-ideal, finite crystal.

$$S(q) = \sum_{h=-N}^{N} \sum_{k=-N}^{N} \sum_{l=-N}^{N} \left| f(h,k,l) \right|^2 \cdot \exp\left[ \frac{-\left(q - QQ(h,k,l)\right)^2}{2w^2} \right]$$

**Equation B1**: Broadened structure factor, in which q: reciprocal space, w: finite size broadening parameter, h,k,l: Miller Indices, N: highest order of reflection, f: summed intensity contribution of one unit cell. Here, N = 5,

$f(h,k,l) = 1 + (-1)^{h+k} + (-1)^{k+l} + (-1)^{l+h}$, and

$$QQ(h,k,l) = \frac{\sqrt{h^2 + k^2 + l^2}}{\sqrt{1^2 + 1^2 + 1^2}} = \frac{\sqrt{h^2 + k^2 + l^2}}{\sqrt{3}}.$$

Introducing another term accounts for disorder within the crystal.

$$S_{disordered}(q) = S(q) \cdot DWF(q)$$

**Equation B3**: Disordered structure factor, in which DWF: Debye-Waller Factor. Here, $DWF(q) = \exp\left(-\sigma^2 \cdot q^2\right)$, in which $\sigma = 0.8$.

In addition, the simulated FCC structure factor was scaled by a constant multiplier and shifted by a constant intensity: $Yscale = 1.056E-7, Yshift = 5.70E-5$

*Appendix C: Determination of Average Gold Nanoparticle Radius*

Based on a set of TEM images (data not shown), the distribution of gold nanoparticle radii could be characterized with image processing software, ImageJ.[16] A histogram was constructed, and the average radius and standard deviation were determined. These values were compared with the values used in the FF simulation (Figure 7, Appendix A).

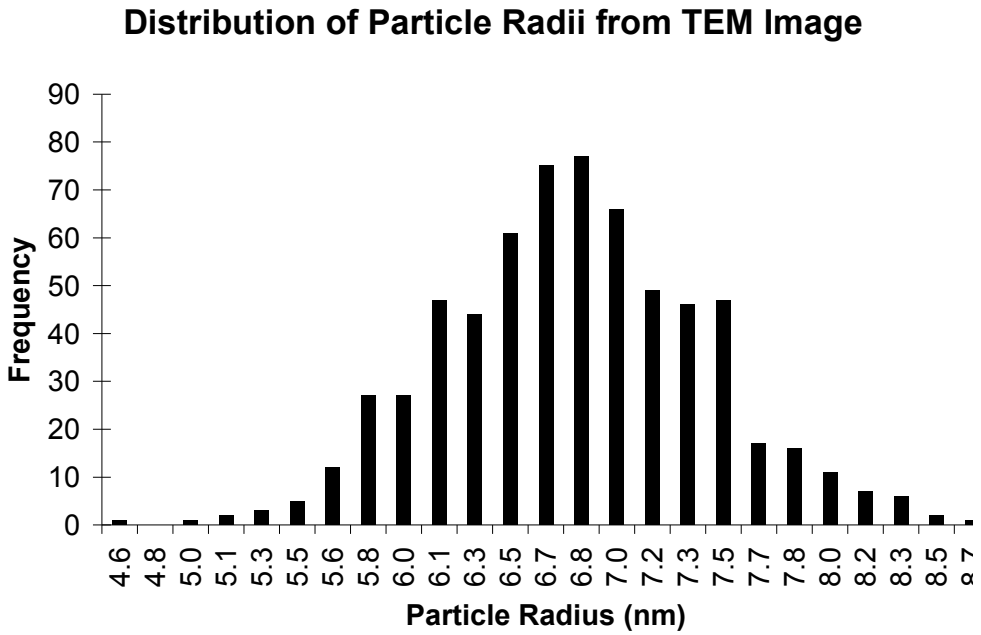


**Figure C1**: Histogram of gold nanoparticle radii. Data from TEM images; a total of ~650 well-spaced particles were characterized. Here, the x-axis refers to the maximum limit of each bin. Based on the data shown here, the average radius was determined as 6.7 ± 0.64 nm.

*Appendix D: Estimation of DNA-Capped Gold Nanoparticle Interparticle Spacing*

Two extreme cases were considered to estimate minimum and maximum values for assembled interparticle spacing, hybridized and unhybridized:

Case 1: Hybridized

(gold nanoparticle diameter) + (two carbon hexamers) + (two unhybridized bases) + (four hybridized bases) = (total interparticle distance);

(12.2 nm) + (2 x 6 x 0.14 nm) + (2 x 0.7 nm) + (4 x 0.34 nm) = 17.3 nm

Case 2: Unhybridized

(gold nanoparticle diameter) + (two carbon hexamers) + (ten unhybridized bases) = (total interparticle distance);

(12.2 nm) + (2 x 6 x 0.14 nm) + (10 x 0.7 nm) = 20.9 nm

REFERENCES


1. Mirkin, C. A., Letsinger, R. L., Mucic, R. C., and Storhoff, J. J., A DNA-based method for rationally assembling nanoparticles into macroscopic materials. *Nature* **382** (6592), 607 (1996).

2. Alivisatos, A. P. et al., Organization of 'nanocrystal molecules' using DNA. *Nature* **382** (6592), 609 (1996).

3. Maye, M. M., Nykypanchuk, D., van der Lelie, D., and Gang, O., A simple method for kinetic control of DNA-induced nanoparticle assembly. *Journal of the American Chemical Society* **128** (43), 14020 (2006).

4. Maye, M. M., Nykypanchuk, D., van der Lelie, D., and Gang, O., DNA-regulated micro- and nanoparticle assembly. *Small* **3** (10), 1678 (2007).

5. Nykypanchuk, D., Maye, M. M., van der Lelie, D., and Gang, O., DNA-guided crystallization of colloidal nanoparticles. *Nature* **451** (7178), 549 (2008).

6. Park, S. Y. et al., DNA-programmable nanoparticle crystallization. *Nature* **451** (7178), 553 (2008).

7. Xiong, H., van der Lelie, D., and Gang, O., DNA linker-mediated crystallization of nanocolloids. *Journal of the American Chemical Society* **130** (8), 2442 (2008).

8. Turkevich, J., Stevenson, P.C., and Hillier, J., A study of the nucleation and growth processes in the synthesis of colloidal gold. *Discussions of the Faraday Society* **11**. (58). 55 (1951).

9. Patterson, A.L., The Scherrer formula for x-ray particle size determination. *Physical Review* **56**. 978 (1939).

10. Warren, B. E. X-ray Diffraction (Addison-Wesley, Reading, Massachusetts, 1969).

11. Cullity, B. D. Elements of X-Ray Diffraction (Addison-Wesley, Reading, Massachusetts, 2001).

12. Glatter, O. & Kratky, O. Small Angle X-ray Scattering (Academic Press, London, England, 1982).

13. Hammersley, A.P., ESRF Internal Report, ESRF98HA01T, FIT2D V9.129 Reference Manual V3.1 (1998).

14. Hammersley, A.P., Svensson, S.O., Hanfland, M., Fitch, A.N., & Häusermann, D., Two-dimensional detector software: from real detector to idealised image or two-theta scan, *High Pressure Research*, **14**. 235, (1996).

15. Rayleigh, Lord, The incidence of light upon a transparent sphere of dimensions comparable with the wavelength. *Proceedings of the Royal Society* (London) **A-84**. 25 (1911).

16. Abramoff, M.D., Magelhaes, P.J., & Ram, S.J. Image Processing with ImageJ. *Biophotonics International*, **11**. 36 (2004).